

1 **Sensitivity of aerosol and cloud properties to coupling strength of**
2 **marine boundary layer clouds over the northwest Atlantic**

3 Kira Zeider¹, Kayla McCauley²⁺, Sanja Dmitrovic³, Leong Wai Siu², Yonghoon Choi^{4,5}, Ewan C.
4 Crosbie^{4,5}, Joshua P. DiGangi⁴, Glenn S. Diskin⁴, Simon Kirschler^{6,7}, John B. Nowak⁴, Michael
5 A. Shook⁴, Kenneth L. Thornhill^{4,5}, Christiane Voigt^{6,7}, Edward L. Winstead^{4,5}, Luke D. Ziemba⁴,
6 Paquita Zuidema⁸, Armin Sorooshian^{1,2,3*}

7 ¹Department of Chemical and Environmental Engineering, University of Arizona, Tucson, AZ, 85721, USA

8 ²Department of Hydrology and Atmospheric Sciences, University of Arizona, Tucson, AZ, 85721, USA

9 ³James C. Wyant College of Optical Sciences, University of Arizona, Tucson, AZ 85721, USA

10 ⁴NASA Langley Research Center, Hampton, VA, 23681, USA

11 ⁵Analytical Mechanics Associates, Hampton, VA, 23666, USA

12 ⁶Institute of Atmospheric Physics, German Aerospace Center, Germany

13 ⁷Institute of Atmospheric Physics, University Mainz, Germany

14 ⁸Rosenstiel School of Marine, Atmospheric, and Earth Science, University of Miami, Miami, FL

15 ⁺Now at EPA, Research Triangle Park, NC 27711

16

17 **Correspondence to:* Armin Sorooshian (armin@arizona.edu)

18 **Abstract**

19 Quantifying the degree of coupling between marine boundary layer clouds and the surface is critical for understanding
20 the evolution of low clouds and explaining the vertical distribution of aerosols and microphysical cloud properties.
21 Previous work has characterized the boundary layer as either coupled or decoupled but this study rather considers four
22 degrees of coupling, ranging from strongly to weakly coupled. We use aircraft data from the NASA Aerosol Cloud
23 meTeorology Interactions oVer western ATlantic Experiment (ACTIVATE) to assess aerosol and cloud characteristics
24 for the following four regimes, quantified using differences in liquid water potential temperature (θ_ℓ) and total water
25 mixing ratio (q_t) between flight data near-surface level (~150 m) and directly below cloud bases: strong coupling ($\Delta\theta_\ell$
26 ≤ 1.0 K, $\Delta q_t \leq 0.8$ g kg⁻¹), moderate coupling with high $\Delta\theta_\ell$ ($\Delta\theta_\ell > 1.0$ K, $\Delta q_t \leq 0.8$ g kg⁻¹), moderate coupling with
27 high Δq_t ($\Delta\theta_\ell \leq 1.0$ K, $\Delta q_t > 0.8$ g kg⁻¹), weak coupling ($\Delta\theta_\ell > 1.0$ K, $\Delta q_t > 0.8$ g kg⁻¹). Results show that (i) turbulence
28 is greater in the strong coupling regime compared to the weak coupling regime, with the former corresponding to more
29 vertical homogeneity in 550 nm aerosol scattering, integrated aerosol volume concentration, and giant aerosol number
30 concentration ($D_p > 3$ μm) coincident with increased MBL mixing; (ii) cloud drop number concentration is greater
31 during periods of strong coupling due to the greater upward vertical velocity and subsequent activation of particles;
32 (iii) sea-salt tracer species (Na^+ , Cl^- , Mg^{2+} , K^+) are present in greater concentrations in the strong coupling regime
33 compared to weak coupling, while tracers of continental pollution (Ca^{2+} , nss-SO_4^{2-} , NO_3^- , oxalate, and NH_4^+) are
34 higher in mass fraction for the weak coupling regime. Additionally, pH and $\text{Cl}^-:\text{Na}^+$ (a marker for chloride depletion)
35 are consistently lower in the weak coupling regime. There were also differences between the two moderate regimes:
36 the moderate, high Δq_t regime had greater turbulent mixing and sea salt concentrations in cloud water, along with
37 smaller differences in integrated volume and giant aerosol number concentration across the two vertical levels
38 compared. This work shows value in defining multiple coupling regimes (rather than the traditional coupled versus
39 decoupled) and demonstrates differences in aerosol and cloud behavior in the MBL for the various regimes.

40

41 **1 Introduction**

42 The composition of marine boundary layer (MBL) cloud properties is strongly linked to the lower troposphere’s
 43 vertical structure, making it critical to understand the degree of coupling between boundary layer clouds and the
 44 ocean’s surface. When the MBL is well-mixed, there is a thermodynamic exchange between the ocean’s surface and
 45 the cloud deck, and it is considered coupled. A decoupled MBL is characterized by a stable layer separating two well-
 46 mixed layers (the cloud deck and sub-cloud layer), preventing exchange between the ocean’s surface and the cloud
 47 base (Nicholls, 1984; Dong et al., 2015; Jones et al., 2011; Wang et al., 2016). Whether the MBL cloud deck is coupled
 48 or decoupled to the surface has potentially important implications for cloud and aerosol properties (Dong et al., 2015;
 49 Wang et al., 2016; Griesche et al., 2021), radiative forcing (Goren et al., 2018), and precipitation (Bretherton et al.,
 50 2010; Dong et al., 2015). Changes in cloud properties and precipitation affect how much solar radiation is reflected to
 51 space (Twomey, 1974; Albrecht, 1989), which in turn affects how much radiative cooling occurs (Ramanathan et al.,
 52 1989).

53
 54 Past studies have investigated coupling behavior of marine stratocumulus due to their relatively high frequency over
 55 the ocean’s surface and strong impact on the Earth’s radiation budget (Zuidema et al., 2009; Jones et al., 2011; Dong
 56 et al., 2015; Wang et al., 2016; Goren et al., 2018). In marine regions, well-mixed moist thermodynamic statistics
 57 indicate coupling of the sub-cloud layer to the surface (Bretherton et al., 1997; Jones et al., 2011; Dong et al., 2015;
 58 Wang et al., 2016; Su et al., 2022). Studies beyond those previously mentioned over the southeast and northeast Pacific
 59 have applied these methods to other regions, such as the Arctic (Griesche et al., 2021) and over land in the Southern
 60 Great Plains of the United States (Su et al., 2022). Table 1 provides a synthesis of previous studies that utilized
 61 thermodynamic statistics for determining coupling, including criteria used, the region in which the study was
 62 conducted, and the cloud types investigated.

63
 64 **Table 1: Summary of coupling criteria and regional conditions from previous work in comparison to this study.**

| Study region; reference | Criteria | Secondary criteria | Layers used | Cloud type |
|---|--|--|--|------------------------------|
| Southeast Pacific; Jones et al. (2011) | Coupled: $\Delta q_t < 0.5 \text{ g kg}^{-1}$ & $\Delta \theta_t < 0.5 \text{ K}$ | Coupled: distance between lifting condensation level (LCL) and cloud base is < 150 m Decoupled: distance > 150 m | Bottom 25% of surface layer to cloud base height | Marine strato- cumulus |
| Azores (Graciosa Island; Northeast Atlantic); Dong et al. (2015) | All other profiles are considered decoupled | | | |
| Northeast Pacific; Wang et al. (2016) | Decoupled: $\Delta q_t > 0.6 \text{ g kg}^{-1}$ & $\Delta \theta_t > 1.0 \text{ K}$ All other clouds are considered coupled | N/A | | |

| | | | | | | |
|--|--|-------------------------------|------------------|---|---|---|
| Southern Great Plains (U.S.); Su et al. (2022) | Coupled: $\Delta\theta_t < 1.0$ K Decoupled: $\Delta\theta_t > 1.0$ K | | | Different Thermodynamic Stability (DTDS) method | Cloud base height minus planetary boundary layer height | Low clouds over land, specifically cumulus |
| Northwest Atlantic; This Study | Degree | Δq_t | $\Delta\theta_t$ | N/A | Below cloud base leg (~100 m below base) minus MinAlt leg (avg. alt ~150 m) | Marine clouds spanning continuum from stratiform to cumulus |
| | Strong | ≤ 0.8 g kg ⁻¹ | ≤ 1.0 K | | | |
| | Moderate, high $\Delta\theta_t$ | ≤ 0.8 g kg ⁻¹ | > 1.0 K | | | |
| | Moderate, high Δq_t | > 0.8 g kg ⁻¹ | ≤ 1.0 K | | | |
| Weak | > 0.8 g kg ⁻¹ | > 1.0 K | | | | |

65
66 As over 45% of the ocean's surface is covered by MBL clouds (Warren et al., 1988), examining relations between
67 aerosol and cloud characteristics with coupling strength is important. Investigation of coupling behavior has not yet
68 been carried out for the northwest Atlantic region, which is a complex thermodynamic region for such work as it is
69 not a classical sub-tropical zone with a stratocumulus cloud deck like most regions investigated in Table 1 (Painemal
70 et al., 2021, 2023). The synoptic conditions over the northwest Atlantic are such that the wintertime has higher cloud
71 fraction with more influence from stratiform boundary layer clouds, whereas the summertime has more trans-Atlantic
72 flow in addition to lower cloud fraction with higher sea surface temperatures promoting shallow cumulus clouds
73 (Painemal et al., 2021). During winter, there is more offshore advection of continental air (Corral et al., 2021;
74 Dadashazar et al., 2021), enhanced precipitation frequency (Painemal et al., 2021), and cold air outbreaks (CAOs), in
75 which cold air is advected across the Gulf Stream front resulting in pronounced differences between air and sea surface
76 temperatures (Brümmer, 1997; Papritz & Spengler, 2015; Seethala et al., 2021). CAOs are typically associated with
77 strong turbulent mixing, leading to the deepening of the boundary layer (Dadashazar et al., 2021; Painemal et al.,
78 2021; Papritz & Spengler, 2015; Tornow et al., 2022). During CAO events, surface wind convergence is driven by
79 horizontal pressure and boundary layer height gradients, contributing to a statically unstable lower troposphere
80 (Painemal et al., 2021; Seethala et al., 2021).

81
82 Motivated by meteorological differences between the northwest Atlantic and other regions in Table 1, the question
83 arises as to whether it is restrictive to consider just the categories of coupled and decoupled clouds; instead, it may be
84 instructive to consider more categories and that they all may have some degree of coupling ranging from weak to
85 strong. This strategy is built off past reports suggesting that the use of the term "decoupled" may not be appropriate
86 and that an MBL can be coupled even though it is poorly mixed (Stevens et al., 1998). The latter case can be viewed
87 as weakly coupled due to episodic updraft-driven convection that is less efficient at mixing the MBL than is the case
88 in well-mixed MBLs in which downdrafts associated with cloud-top radiative cooling couple the cloud and sub-cloud
89 layers (Stevens et al., 1998). Thus, the perspective we embrace in this work is that low-level clouds (< 2 km) can be
90 viewed as always being coupled to sub-cloud layers but to varying degrees.

91

92 The goal of this study is to leverage an opportune aircraft dataset covering multiple seasons between 2020 to 2022
93 from NASA's Aerosol Cloud meteorology Interactions over the western Atlantic Experiment (ACTIVATE;
94 Sorooshian et al., 2019) to quantify the frequency of occurrence for four different coupling regimes and how aerosol
95 and cloud characteristics vary between them. We emphasize that this study is different in nature to those in Table 1 in
96 that we do not examine as rigorously the vertical extent of the full cloudy boundary layer but instead focus more on
97 aerosol and cloud characteristics for different coupling regimes based on definitions limited to the vertical region
98 below cloud bases. The analyses presented here are important for reasons such as knowing how well the aerosol near
99 the surface level represent the aerosol just below cloud bases, with implications for the aerosol that largely govern the
100 drop concentration budget. In Sect. 2 we summarize the measurements and methods, including criteria applied with
101 traditionally used thermodynamic variables to differentiate between four coupling categories. In Sect. 3 we report
102 results including the frequency of occurrence of the four coupling regimes, and differences in aerosol properties (light
103 scattering, number/volume concentration) and cloud microphysical properties (composition and droplet number
104 concentration) between these categories to see how they compare to past studies for other regions. Although there are
105 scarce previous reports of such findings (e.g., Dong et al., 2015; Wang et al., 2016), the central hypotheses are based
106 on confirming what has been shown or implied in other regions, in that more strongly coupled cases will have (i) more
107 vertical homogeneity in aerosol properties between the sub-cloud layer and closer to the ocean's surface, (ii) cloud
108 composition reflecting significantly more sea salt influence (Wang et al., 2016), and (iii) higher cloud drop number
109 concentration, compared to weakly coupled cases (Dong et al., 2015). Differences identified in aerosol and cloud
110 characteristics between these four coupling regimes are important to inform both future flight designs and data analysis
111 research to account for thermodynamic profiles when examining aspects of aerosol and cloud microphysics when
112 using either satellite, reanalysis, airborne, or ground-based datasets.

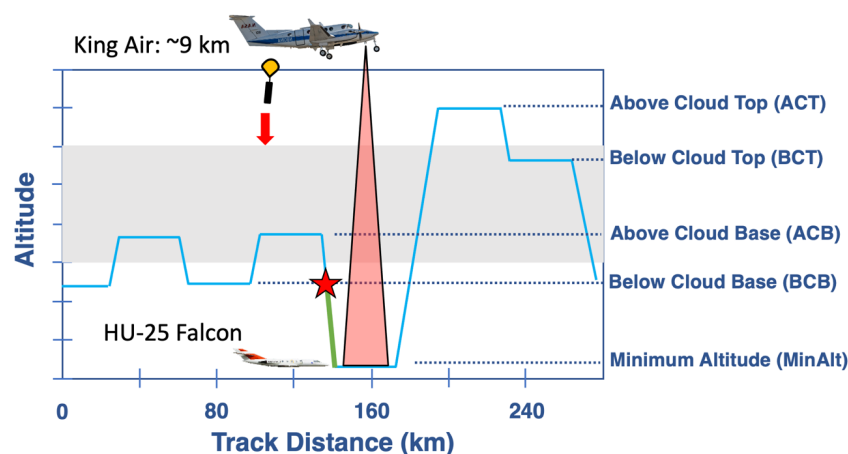
113

114 **2 Data and Methodology**

115 **2.1 Overview of ACTIVATE**

116 ACTIVATE was largely based out of NASA Langley Research Center in Hampton, Virginia and carried out research
117 flights (RFs) with two spatially coordinated aircraft as part of six deployments in winter and summer months between
118 2020 and 2022, with extensive measurement and deployment details provided elsewhere (Sorooshian et al., 2023).
119 Secondary bases were used for a subset of flights in 2022, including in Bermuda for June 2022. Winter and summer
120 are broadly defined as including the months of November-April and May-September, respectively. The HU-25 Falcon
121 flew level legs in, below, and above MBL clouds to collect in-situ atmospheric state, aerosol, trace gas, and cloud
122 measurements, while the high-flying King Air at ~9 km launched dropsondes and carried out remote sensing. The
123 focus of this work is data collected by the Falcon. Out of 179 total flights, 135 were used that offered data conducive
124 to this study's analysis including having the Falcon conduct "statistical survey" flights with "cloud ensembles" (Fig.
125 1), along with several physical conditions satisfied as discussed in Sect. 2.5. During statistical survey flights, which
126 accounted for 93% of ACTIVATE's flights, the Falcon repeatedly flew a series of legs with Fig. 1 visually depicting
127 one such cloud ensemble whereby the plane flew the following legs in this nominal order: two pairs of legs below
128 cloud base (BCB) and above cloud base (ACB) followed by a descent to the minimum altitude (MinAlt) possible

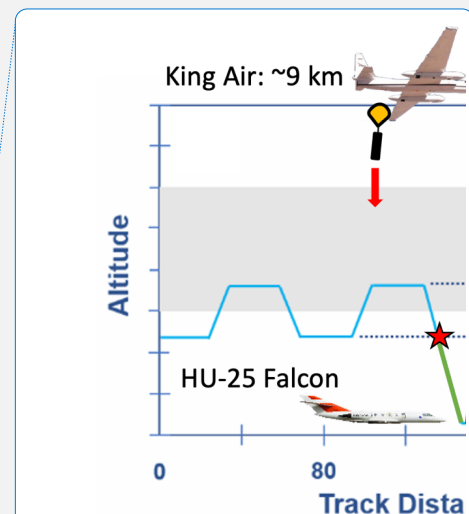
129 (~150 m above sea level) and then a subsequent slant ascent for a leg above cloud top (ACT) followed by a final leg
 130 below cloud top (BCT). Sometimes the legs were flown in a different order based on flight restrictions and cloud
 131 conditions. Separate ensembles flown in clear air conditions are outside the scope of this work. Each leg duration was
 132 ~3.3 minutes (equivalent to ~ 24 km) with the Falcon flying at ~120 m s⁻¹ (Dadashazar et al., 2022a). The vertical
 133 slant ascents/descents between level legs especially down to MinAlt and up to ACT were helpful in gathering
 134 vertically-resolved information during ensembles.
 135



136
 137 Figure 1: Cloudy ensemble flight strategy of the HU-25 Falcon during the ACTIVATE flights, where the grey box represents
 138 a typical cloud layer. The red star indicates where the BCB level would be marked and the data that would be utilized for
 139 this particular flight pattern. Otherwise, MinAlt-BCB pairs that are used include when a MinAlt level leg was immediately
 140 preceded or succeeded by a BCB level leg. The green line illustrates the data that would be used to investigate the vertical
 141 structure of the layer, starting with the last timestamp from the pseudo-BCB leg and ending with the first timestamp in the
 142 MinAlt leg.
 143

144 2.2 Implementation of Flight Legs

145 Across ACTIVATE's six deployments, MinAlt and BCB legs were identified for RFs when the Falcon flew cloud
 146 ensembles (Fig. 1). There were several instances when the MinAlt and BCB legs were not immediately adjacent and
 147 separated by another leg, such as at ACB (i.e., the flight order was BCB-ACB-MinAlt; Fig. 1). In those cases, to get
 148 MinAlt/BCB pairs that were closer in time, our method involved identifying the BCB altitude during the slant
 149 altitudinal change (either descent or ascent) between MinAlt-ACB based on the altitude of the BCB leg immediately
 150 before the ACB leg (see red star in Fig. 1). A secondary check was made to ensure that identified BCB leg was below
 151 cloud base using 1-Hz LWC and N_d values from the FCDP (criteria in Sect. 2.5). The vertical structure of the layer
 152 between MinAlt and BCB was examined using data between the last time stamp in the MinAlt/BCB leg (i.e.,
 153 whichever was first in the MinAlt-BCB pair) and first-time stamp in the subsequent BCB/MinAlt leg (i.e., whichever



Deleted:

Deleted: with upper and lower boundaries representing cloud top and base, respectively. The order of legs was the nominal plan that was flown, but sometimes the legs were flown in a different order based on flight restrictions and cloud conditions.

Deleted: , which is during the slant descent from ACB to MinAlt and uses the mean altitude of the preceding BCB leg immediately before the ACB leg; that level would then be compared to the adjacent MinAlt level that begins at the end of the slant descent

165 was second in the MinAlt-BCB pair). This is indicated by a green line on Fig. 1, which begins with the last time stamp
 166 from the pseudo-BCB leg (indicated by the red star) and ends with the first time stamp in the MinAlt leg. For
 167 simplicity, we refer to the case of using BCB data during slant profiles as “legs” too, even though they were not level
 168 legs. This study compares various measurement data (Sect. 2.5) between MinAlt and BCB legs using the last/first 5
 169 seconds of data during adjacent MinAlt-BCB legs, and in the case of slants, we use the 2 points before and after the
 170 actual BCB point (the red star in Fig. 1) for a total of 5 points (average altitude range ~ 20 m) that represent the BCB
 171 level with the condition that all data were out of cloud.

172

173 2.3 Instrumentation

174 A summary of instrumentation relevant to this study is shown in Table 2 and briefly described here. A nephelometer
 175 (TSI-3563) measured the dry scattering coefficient at 550 nm (particle diameter (D_p) < 5.0 μm for 2020 and D_p < 1.0
 176 μm for 2021 and 2022); a Laser Aerosol Spectrometer (LAS; TSI-3340) measured aerosol size distributions (0.1 μm
 177 < D_p < 5.0 μm) and here we use the integrated aerosol volume concentration data; a Fast Cloud Droplet Probe (FCDP;
 178 SPEC Inc.) measured liquid water content (LWC) and particle and cloud drop size distributions between 3 and 50 μm ;
 179 a two-dimensional stereo (2D-S; SPEC Inc.; 25 μm < D_p < 1500 μm) probe provided LWC, liquid droplet effective
 180 diameter, and an ice flag, where the ice flag is equal to 1 if ice was detected (otherwise the variable is equal to 0); a
 181 diode laser hygrometer (DLH) measured the water vapor mixing ratio (q_p); a turbulent air motion measurement system
 182 (TAMMS) measured three-dimensional winds (Thornhill et al., 2003); and an axial cyclone cloud water collector
 183 (AC3) (Crosbie et al., 2018) collected cloud water samples by inertially separating droplets from the air stream.
 184 Collected cloud water samples were then analyzed post-flight with ion chromatography (IC) with operating conditions
 185 summarized elsewhere (Corral et al., 2022; Gonzalez et al., 2022). Section 2.6 describes the cloud water data in more
 186 detail.

187

188 **Table 2: Summary of field campaign instrumentation used and corresponding measurements.**

| Instruments | Measurements (Uncertainty) | Diameter (μm) | Reference |
|--|---|--|-------------------------|
| TSI-3563 Nephelometer | Dry scattering coefficient at 550 nm (20%) | < 5.0 for 2020; < 1.0 for 2021 & 2022 | Ziemba et al. (2013) |
| TSI-3340 Laser Aerosol Spectrometer (LAS) | Integrated aerosol volume concentration (20%) | 0.1 – 5.0 | Froyd et al. (2019) |
| SPEC Inc. Fast Cloud Droplet Probe (FCDP) | Liquid water content (LWC), particle number concentration (N_a), cloud drop number concentration (N_d) (15-50%) | 3 – 50 | Kirschler et al. (2022) |
| SPEC Inc. Two-Dimensional Stereo Probe, Horizontal Arm (2DS-H) | LWC, effective diameter for liquid, ice flag (15-50%) | 25 – 1500 | Kirschler et al. (2023) |

| | | | |
|---|---|---------------|-------------------------|
| Diode Laser Hygrometer (DLH) | Water vapor mixing ratio (q_v) (5%) | N/A | Diskin et al. (2002) |
| Axial Cloud Water Collector (AC3) | Cloud water composition ($< 20\%$, species dependent) | see Sect. 2.6 | Crosbie et al. (2018) |
| Turbulent Air Motion Measurement System (TAMMS) | Three dimensional winds ($w = 10 \text{ cm s}^{-1}$; $u, v = 50 \text{ cm s}^{-1}$) and temperature ($0.5 \text{ }^\circ\text{C}$) | N/A | Thornhill et al. (2003) |

189

190

191 2.4 Marine Boundary Layer Coupling

192 2.4.1 Thermodynamic Variables

193 To estimate the degree of coupling within the marine boundary layer, we consider the change in vertical profile of two
194 parameters: total water mixing ratio (q_t) and liquid water potential temperature (θ_t). Relevant to this study are these
195 equations,

196

$$197 q_\ell = \frac{LWC}{\rho_d} \quad (1)$$

198

$$199 q_t = q_v + q_\ell \quad (2)$$

200

201 where the total water mixing ratio is the sum of water vapor mixing ratio (q_v) and liquid water mixing ratio (q_ℓ). The
202 water vapor mixing ratio (q_v) provided by the DLH is converted from ppmv to g kg^{-1} . The liquid water mixing ratio
203 (q_ℓ) is defined as the ratio of the mass of liquid water to the mass of dry air within a unit volume of air, which is
204 equivalent to the ratio of LWC (provided by the FCDP) and the density of dry air (ρ_d).

205 Also relevant are these equations,

206

$$207 \theta = (T + 273.15) \times \left(\frac{p_0}{p}\right)^\kappa \quad (3)$$

208

$$209 \theta_\ell = \theta - \left(\frac{L_v}{c_{pd}}\right) \times q_\ell \quad (4)$$

210

211 where in equation 3, T and p are the given temperature in $^\circ\text{C}$ and pressure in hPa from Falcon measurements,
212 respectively, p_0 is the reference pressure (= 1000 hPa), and κ is the ratio of gas constant of dry air (R_d) to the specific
213 heat of dry air at constant pressure (c_{pd}). In equation 4, L_v is latent heat of vaporization and c_{pd} is the specific heat of
214 dry air at constant pressure. When LWC is equal to 0, θ_ℓ is equal to θ . θ_ℓ is useful for the purposes of this study as it
215 is not significantly influenced by evaporating precipitation. Information regarding LWC thresholds for MinAlt-BCB
216 pairs is included in Sect. 2.5.

217

218 For each MinAlt and BCB leg, the average θ_t and q_t across the leg was calculated and the difference between the two
 219 layers was taken as follows:

$$220 \Delta q_t = q_{t,MinAlt} - q_{t,BCB^*} \quad (5)$$

$$221 \Delta \theta_t = \theta_{t,BCB^*} - \theta_{t,MinAlt} \quad (6)$$

222 where in both equations 5-6, the order of legs on the right-hand side is meant to arrive at a positive value for the
 223 difference based on expectation.

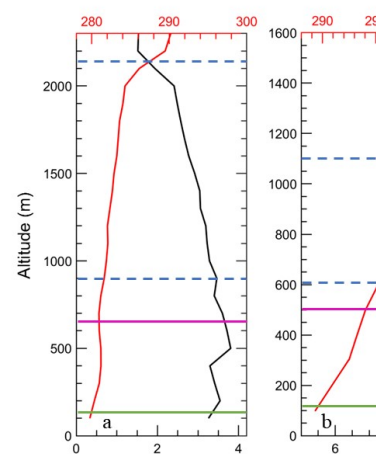
224 2.4.2 Coupling Criteria

225 The criteria we use for the different coupling regimes were informed by (but are not identical to) those used in past
 226 work (Jones et al., 2011; Dong et al., 2015; Wang et al., 2016; Su et al., 2022). Our focus was on comparing the vertical
 227 range between MinAlt and BCB legs due to the focus on examining aerosol characteristics in particular within that
 228 range and also cloud microphysical conditions above cloud base. To qualify as strongly coupled, the difference
 229 between MinAlt and BCB had to satisfy these conditions: $\Delta q_t \leq 0.8 \text{ g kg}^{-1}$ and $\Delta \theta_t \leq 1.0 \text{ K}$ (example in Fig. 2a). Since
 230 Δq_t is more influenced by evaporation and condensation, whereas $\Delta \theta_t$ is more affected by air mass mixing (such as
 231 entrainment) and diabatic heating and cooling, it is proposed to have two degrees of moderate coupling – when one
 232 of Δq_t and $\Delta \theta_t$ fit the strong coupling criteria and the other did not (Fig. 2b-c). Finally, profiles are considered “weakly
 233 coupled” when both Δq_t and $\Delta \theta_t$ do not satisfy the strong coupling criteria values (Fig. 2d). Vertical profiles of q_t and
 234 θ_t were examined for all MinAlt/BCB pairs to ensure robustness of the categorization method. As noted by Dadashazar
 235 et al. (2022b), the Falcon aimed to conduct BCB and ACB legs about ~100 m below and above the estimated cloud
 236 base height, respectively. Median/mean distances from BCB to cloud bases were as follows for all samples in the four
 237 coupling categories: strong = 73/87 m; moderate, high $\Delta \theta_t$ = 101/119 m; moderate, high Δq_t = 69/71 m; weak =
 238 104/142 m. The use of the two moderate categories is exploratory in nature and meant to identify if differences are
 239 found between both themselves and the more extreme categories of strong and weak. Appendix A further explores
 240 differences between the two moderate regimes and suggests that the moderately coupled category with high $\Delta \theta_t$ is
 241 influenced more by processes above the MBL such as entrainment of dry air with high potential temperature whereas
 242 the other moderate category with high Δq_t is influenced by surface processes.

243

Deleted: We note that while Fig. 2a/d show BCB legs being relatively farther below the actual cloud base height (Fig. 2a = 223 m; Fig. 2d = 370 m) than the other two examples (Fig. 2b = 101 m; Fig. 2c = 30 m), the former two were anomalous cases and usually the BCB legs were closer to cloud base.

Formatted: Font color: Text 1, Kern at 12 pt



Deleted:

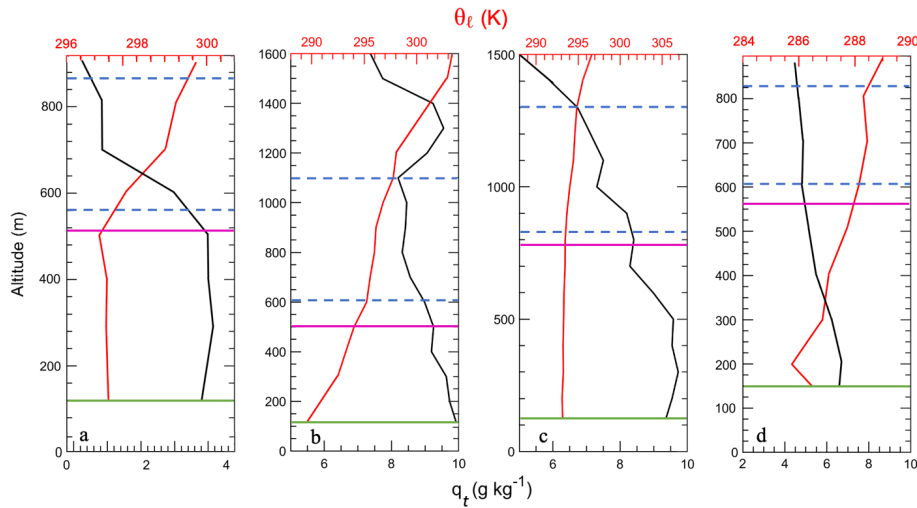


Figure 2: Representative vertical profiles of θ_l and q_t for (a) strong coupling from RF 26 on 21 August 2020, (b) moderate coupling with high $\Delta\theta_l$ from RF 150 on 5 May 2022, (c) moderate coupling with high Δq_t from RF 66 on 18 May 2021, and (d) weak coupling from RF 41 on 28 February 2020. The dashed blue lines demarcate the cloud top and base levels, the magenta line indicates the BCB leg, and the green line indicates the MinAlt leg. There was a total of 411 MinAlt-BCB pairs analyzed in this study.

2.5 Aerosol and Atmospheric Properties

There were several aerosol and atmospheric properties investigated in this study: aerosol scattering (scat) at 550 nm ($< 5 \mu\text{m}$ in 2020 and $< 1 \mu\text{m}$ in 2021-2022), integrated volume concentration (IntV : $0.1 < D_p < 5 \mu\text{m}$), particle number concentration (N_a ; $3 < D_p < 50 \mu\text{m}$), cloud drop number concentration (N_d ; $3 < D_p < 50 \mu\text{m}$), and turbulence (σ_w). Note that the N_a measurement from the FCDP for diameter $> 3 \mu\text{m}$ is important in this study to better isolate sea salt particles (Gonzalez et al., 2022). The integrated volume concentration also is expected to be influenced by larger sea salt particles in the measurement size range. These properties were averaged across each MinAlt and BCB pair and the difference between the MinAlt and BCB values was computed. To account for interference from cloud droplet shatter with the aerosol statistics, we only looked at MinAlt-BCB pairs when the sampling area was devoid of cloud, rain, and ice. The following three criteria had to be met: (1) ice flag from 2DS-H = 0, (2) effective liquid diameter from 2DS-H $< 60 \mu\text{m}$, and (3) LWC from FCDP $< 0.005 \text{ g m}^{-3}$, to filter out conditions with ice, liquid precipitation, and clouds, respectively. When considering in-cloud conditions for N_d , additional criteria were needed based on FCDP data: LWC $> 0.05 \text{ g m}^{-3}$ and $N_d > 10 \text{ cm}^{-3}$ (Kirschler et al., 2023). N_d data was collected from ACB legs closest in proximity to a MinAlt-BCB pair ($< 30 \text{ min}$; 60% within 10 min) due to one of the study objectives being to examine how N_d varies between the four defined coupling regimes. Turbulence was calculated as the standard deviation of the vertical wind velocity for a level leg as done in other work (e.g., MacDonald et al., 2020).

Deleted: 44

Deleted: 3 February 2021

Deleted: 158

Deleted: 20 May 2022.

281
282 **2.6 Cloud Water Species**
283 The nine cloud water species of interest in this study include non-sea salt calcium (nss-Ca²⁺), chloride (Cl⁻), potassium
284 (K⁺), magnesium (Mg²⁺), sodium (Na⁺), ammonium (NH₄⁺), nitrate (NO₃⁻), oxalate, and non-sea salt sulfate (nss-
285 SO₄²⁻). Calculations of nss-Ca²⁺ and nss-SO₄²⁻ utilized mass ratios and concentrations of pure Ca²⁺, Na⁺, and SO₄²⁻,
286 following the methodology outlined in Sect. 2.7 of AzadiAghdam et al. (2019). The IC is used to obtain concentrations
287 of cloud water species in aqueous units (mg L⁻¹), which were then converted to air equivalent concentrations using the
288 methods described in Gonzalez et al. (2022). Briefly, the cloud water sample was considered in-cloud under the criteria
289 LWC_{FCDP} > 0.05 g m⁻³. When this condition was met, the concentration was multiplied by the average LWC_{FCDP}
290 measured across the sampling time and divided by the density of water and ultimately converted to µg m⁻³ for the air
291 equivalent concentration. These units allow one to compare concentrations more fairly between samples to remove
292 biases due to varying amounts of water in different clouds. As cloud water samples were collected periodically during
293 flights, samples were only examined when a MinAlt or BCB leg being investigated was within 30 minutes or
294 overlapped with the collection period. Out of a total of 535 cloud water samples over the 6 deployments, 67 met the
295 criteria to be used for this study's MinAlt/BCB pairs. Statistics including mean, standard deviation (std. dev.),
296 minimum, maximum, and quartile ranges were calculated across the 67 data points for all nine cloud water species.

297
298 Additionally, cumulative average cloud water mass concentrations and mass fractions were calculated for the 67
299 samples. The total mass concentration for each coupling regime was found by the summation of only the nine chemical
300 species investigated in this manuscript. Welch's t-test calculations were conducted to compare the mean concentrations
301 of the investigated chemical species across coupling regimes. These tests were done in lieu of the traditional t-test due
302 to the assumption that the data used have unequal variances and thus are slightly more robust.

303

304 **3 Results and Discussion**

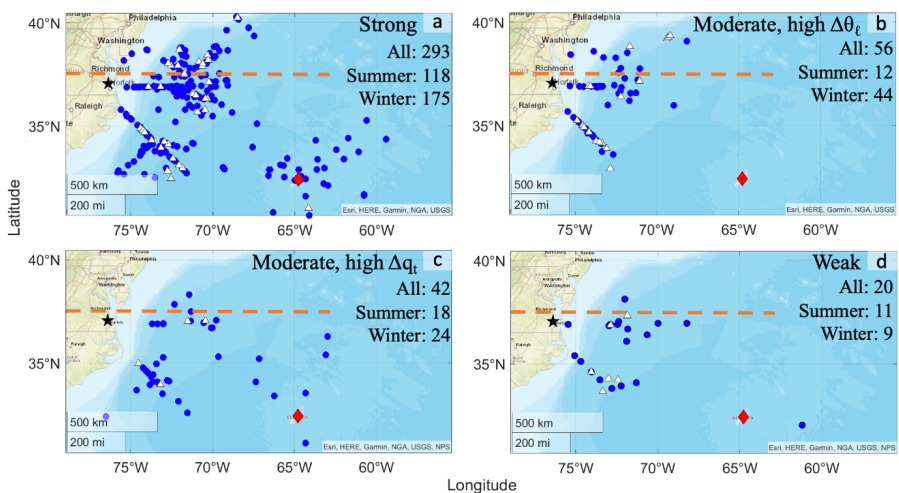
305 **3.1 Thermodynamic Criteria**

306 This section discusses the application of the developed thermodynamic criteria across all MinAlt-BCB pairs. In total,
307 411 MinAlt-BCB pairs were investigated (pair locations shown in Fig. 3; [the MinAlt legs were close in time to the](#)
308 [BCB legs, so only one spatial map is needed to show the approximate data point location for each pair](#)), with the
309 breakdown of the distribution across the different degrees of coupling shown in Fig. 3 and 4. The majority of the pairs
310 were classified as strongly coupled, with a breakdown of 71% (strongly coupled), 14% (moderately coupled with high
311 $\Delta\theta_v$), 10% (moderately coupled with high Δq), and 5% (weakly coupled). Strong turbulent mixing in the northwest
312 Atlantic Ocean, especially during the winter (Brunke et al., 2022) which is when most pairs were identified, is likely
313 why the majority of pairs were found to be strongly coupled, as the coupling parameters θ_v and q_r are relatively constant
314 vertically from the surface to near cloud bases due to the strong mixing (Fig. 2a).

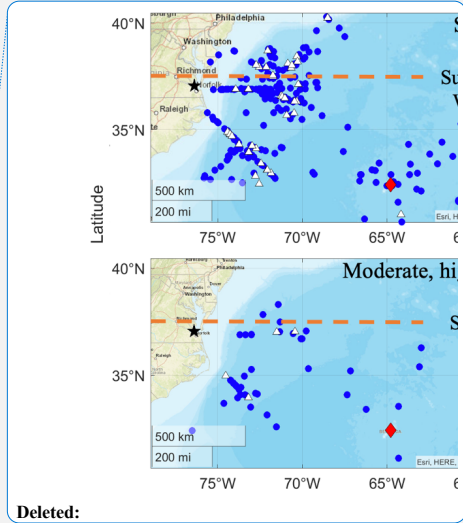
315

316 There are no major spatial distribution differences for MinAlt-BCB pairs across the four coupling regimes with minor
317 exceptions being that the majority of pairs identified farther offshore around Bermuda were for both the strongly

318 coupled and moderately coupled with high Δq categories. Also, the strong and moderate coupling with high $\Delta\theta_t$
 319 categories had more pairs north of 37.5°N (indicated by the orange dashed line), which coincides with more wintertime
 320 sampling of cold air outbreak events that feature turbulent conditions (e.g., Painemal et al., 2021; Kirschler et al.,
 321 2022).
 322



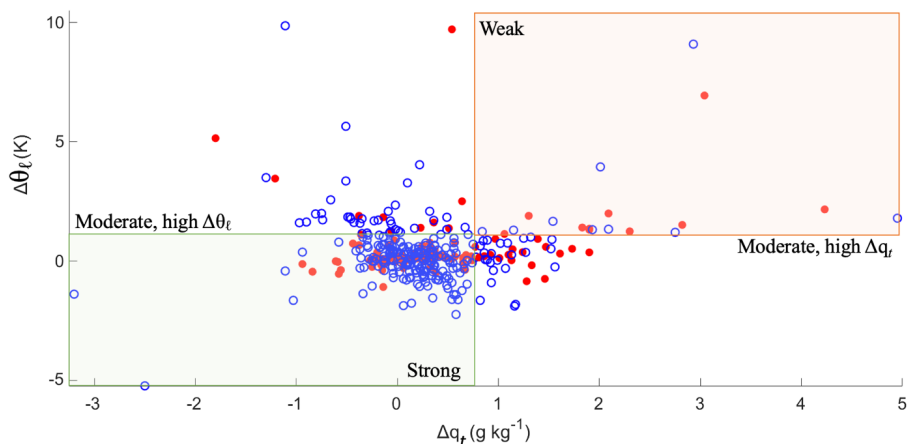
323
 324 **Figure 3: Locations of the BCB segments of the MinAlt-BCB pairs (blue circles), broken up into the four different degrees**
 325 **of coupling. The locations of the cloud water samples (white triangles) are overlaid on the BCB segment locations. The black**
 326 **star indicates the location of NASA Langley Research Center, the red diamond indicates Bermuda, and the orange dashed**
 327 **line indicates 37.5°N, which is referenced in the discussion about this figure. The total number of MinAlt-BCB pairs for**
 328 **each category are also included for each coupling regime.**
 329



Deleted:

Deleted: The MinAlt legs were close in time to the BCB legs, so only one spatial map is needed to show the approximate data point location for each pair.

Deleted: The winter months include January, February, March, and April, while the summer months include May, June, August, and September.



337
 338 **Figure 4: Scatterplot of $\Delta\theta_e$ vs. Δq_e values for the BCB and MinAlt pairs divided into the four coupling regimes, where**
 339 **winter pairs are indicated by blue points and summer pairs are indicated by red points. Refer to Fig. 3 for the number of**
 340 **points in each coupling regime categorized by season. Figure S1 shows this information in the form of a joint frequency**
 341 **histogram.**

342
 343 Figures 3-4 show that there were more MinAlt-BCB pairs during the winter versus summer (252 vs. 159) largely due to the
 344 greater ease of sampling such cases with the higher wintertime cloud fraction in the region (Painemal et al., 2021;
 345 Kirschler et al., 2022, 2023). But generally, the distribution of coupling categories was the same (summer/winter):
 346 74/70% strongly coupled, 8/18% moderately coupled with high $\Delta\theta_e$, 11/10% moderately coupled with high Δq_e , and
 347 7/4% weakly coupled. The frequency of the moderately coupled with high Δq_e category was relatively higher in
 348 summer versus winter compared to the other moderate category, which is coincident with the summer having higher
 349 temperatures (i.e., higher q_e) and more flights farther south in Fig. 3 where temperatures are warmer as compared to
 350 farther north.

351
 352 For context, applying the criteria from past work in Table 1 (Jones et al., 2011; Dong et al., 2015) to this dataset (i.e.,
 353 Δq_e [g kg^{-1}] and $\Delta\theta_e$ [K] < 0.5 for coupled and all others decoupled) would have led to 206 and 205 coupled and
 354 decoupled cases, respectively, with a seasonal breakdown as follows (summer/winter): 43/58% coupled, 35/66%
 355 decoupled. However, we caution that the compared vertical levels differ between these studies. For example, Jones et
 356 al. (2011) compared levels encompassing more of the full extent of the cloudy MBL (e.g., somewhat analogous to the
 357 use of MinAlt and BCT in Fig. 1), whereas in this study we compare MinAlt to BCB due to our focus on aerosol
 358 characteristics, which are difficult to measure in clouds. While ACTIVATE flights were designed for achieving a
 359 statistically rich dataset portraying the region in an unbiased way, the frequency of occurrence of the four coupling
 360 regimes in this study can possibly still be affected by how flights were designed to fly towards areas with relatively

361 higher cloud fraction without complicating scenes such as with multiple cloud layers. We also note that sensitivity
 362 tests were conducted (Table S1) to see how the assignment of MinAlt-BCB pairs to the four coupling categories
 363 changed when accounting for measurement uncertainties (shown in Table 2), which could push points across the
 364 border of their regime in Fig. 4. Varying Δq_t and $\Delta \theta_t$ by absolute values of 0.2 in both directions was investigated to
 365 test for sensitivity to measurement uncertainty in this study. Results are preserved with only slight changes in
 366 assignments after varying the criteria; the same applies using the Jones et al. (2011) criteria, which is shown on the
 367 far right of Table S1. Subsequent effects on other results presented in the following sections were minimal with the
 368 same general conclusions reached.

369

370 3.2 Aerosol and Atmospheric Properties

371 The results of the aerosol and atmospheric parameter calculations across the four different coupling regimes are
 372 provided in Table 3 (seasonal results in Tables S2-S3), with notched box plots summarizing information from Table 3
 373 in Fig. S2. Of the 411 MinAlt-BCB pairs, 293 were used in aerosol calculations after eliminating pairs that may have
 374 been influenced by rain, cloud, or ice interference. As a note, when quantifying altitudinal differences in variables
 375 across different coupling regimes, the mean at each altitude is used as the comparison parameter unless otherwise
 376 stated, as outliers were already removed prior to data analysis.

377

378 The first hypothesis of this study is that strongly coupled regimes would have greater turbulence (σ_w) than weakly
 379 coupled regimes. This hypothesis is confirmed when examining σ_w results at both MinAlt (strong/weak = 0.86/0.55
 380 m s^{-1}) and BCB levels (strong/weak = 0.70/0.49 m s^{-1}). The two categories of moderate coupling had greater turbulence
 381 at both altitudes compared to weak coupling, and sometimes had greater turbulence than pairs categorized as strongly
 382 coupled. Further, while BCB σ_w and BCB – MinAlt σ_w had no significant differences across medians, there were some
 383 significant differences across σ_w coupling regimes for MinAlt σ_w (Fig. S2). Data in the moderate, high $\Delta \theta_t$ coupling
 384 regime were significantly different from the other regimes, and data categorized as moderate coupling with high Δq_t
 385 were also statistically distinct from the weak coupling regime. This suggests considering multiple coupling regimes
 386 for the northwest Atlantic is important to tease out such nuances as differences in the thermodynamic profiles can
 387 potentially coincide with different aerosol and cloud characteristics as discussed subsequently.

388

389 **Table 3: Statistics for various atmospheric properties investigated across the MinAlt-BCB pairs (Δ calculation refers to the**
 390 **MinAlt value minus the BCB value), except for MinAlt σ_w and BCB σ_w , which are the average σ_w for each respective leg**
 391 **and for N_a , which is calculated in ACB legs. Each property is broken down into the different degrees of coupling (n = number**
 392 **of points used in each coupling category). Variable acronyms defined in Sect. 2.5. Refer to Fig. S2 for corresponding notched**
 393 **box plots.**

| | Degree of Coupling | Mean | Std. Dev. | Min | 25% | 50% | 75% | Max | n |
|------------------------|----------------------------------|------|-----------|------|------|-----|-----|------|-----|
| Δ_{scat} | Strong | 2.2 | 2.1 | 0.00 | 0.78 | 1.7 | 2.8 | 13.9 | 274 |
| | Moderate, high $\Delta \theta_t$ | 3.5 | 3.5 | 0.07 | 0.97 | 2.4 | 4.6 | 14.6 | 52 |
| | Moderate, high Δq_t | 2.4 | 2.1 | 0.01 | 0.70 | 1.8 | 3.6 | 9.2 | 39 |
| | Weak | 3.5 | 3.3 | 0.01 | 0.88 | 2.2 | 6.6 | 10.8 | 20 |

Deleted: ,

Deleted: 4.

Deleted: for Δq_t and $\Delta \theta_t$ by absolute values of 0.02 in both directions

| | | | | | | | | | |
|----------------------------|------------------------------------|-------|------|------|-------|-------|------|------|-----|
| ΔIntV | Strong | 2.5 | 2.6 | 0.02 | 0.67 | 1.7 | 3.5 | 13.6 | 288 |
| | Moderate, high $\Delta\theta_\ell$ | 2.1 | 2.2 | 0.00 | 0.46 | 1.5 | 2.9 | 9.3 | 54 |
| | Moderate, high Δq_f | 1.9 | 1.9 | 0.01 | 0.46 | 1.2 | 2.8 | 8.3 | 41 |
| | Weak | 2.8 | 2.3 | 0.18 | 1.0 | 2.4 | 4.2 | 7.6 | 20 |
| $\Delta N_{>3\mu\text{m}}$ | Strong | 0.32 | 0.55 | 0.00 | 0.05 | 0.13 | 0.35 | 4.9 | 288 |
| | Moderate, high $\Delta\theta_\ell$ | 0.33 | 0.64 | 0.00 | 0.03 | 0.13 | 0.31 | 3.6 | 54 |
| | Moderate, high Δq_f | 0.15 | 0.14 | 0.00 | 0.06 | 0.11 | 0.21 | 0.61 | 41 |
| | Weak | 0.53 | 1.5 | 0.01 | 0.02 | 0.08 | 0.27 | 5.9 | 20 |
| N_d | Strong | 344 | 217 | 19 | 193 | 310 | 473 | 954 | 238 |
| | Moderate, high $\Delta\theta_\ell$ | 419 | 242 | 45 | 228 | 374 | 610 | 962 | 48 |
| | Moderate, high Δq_f | 329 | 154 | 25 | 235 | 327 | 430 | 671 | 31 |
| | Weak | 275 | 181 | 50 | 107 | 245 | 411 | 606 | 18 |
| MinAlt σ_w | Strong | 0.86 | 0.49 | 0.00 | 0.47 | 0.79 | 1.2 | 2.4 | 293 |
| | Moderate, high $\Delta\theta_\ell$ | 1.0 | 0.57 | 0.00 | 0.52 | 1.1 | 1.3 | 2.2 | 56 |
| | Moderate, high Δq_f | 0.81 | 0.44 | 0.00 | 0.51 | 0.73 | 0.99 | 1.9 | 42 |
| | Weak | 0.55 | 0.38 | 0.00 | 0.19 | 0.51 | 0.90 | 1.3 | 20 |
| BCB σ_w | Strong | 0.70 | 0.62 | 0.00 | 0.26 | 0.60 | 1.0 | 4.0 | 293 |
| | Moderate, high $\Delta\theta_\ell$ | 0.64 | 0.62 | 0.00 | 0.00 | 0.53 | 1.1 | 2.2 | 56 |
| | Moderate, high Δq_f | 0.81 | 0.76 | 0.00 | 0.26 | 0.71 | 1.1 | 3.3 | 42 |
| | Weak | 0.49 | 0.50 | 0.00 | 0.04 | 0.30 | 0.87 | 1.6 | 20 |
| BCB - MinAlt σ_w | Strong | -0.15 | 0.66 | -2.0 | -0.45 | -0.16 | 0.10 | 3.6 | 285 |
| | Moderate, high $\Delta\theta_\ell$ | -0.34 | 0.57 | -2.2 | -0.81 | -0.23 | 0.10 | 0.59 | 53 |
| | Moderate, high Δq_f | 0.01 | 0.74 | -1.6 | -0.28 | -0.08 | 0.20 | 2.9 | 42 |
| | Weak | -0.05 | 0.47 | -1.1 | -0.35 | 0.01 | 0.25 | 0.90 | 20 |

398

399 The second hypothesis is that aerosol scattering (Δscat), integrated volume concentration ($0.1 < D_p < 5 \mu\text{m}$; ΔIntV),
400 and giant particle number concentration ($3 < D_p < 50 \mu\text{m}$; $\Delta N_{>3\mu\text{m}}$) would have more vertically homogenous
401 concentrations (i.e., smaller MinAlt-BCB differences) in strongly coupled regimes compared to weakly coupled
402 regimes due to greater mixing for the former as supported by the higher σ_w results already shown. This hypothesis is
403 supported (Table 3 and Fig. S2) since strong coupling cases exhibited lower mean differences (MinAlt-BCB) than
404 weak coupling (Δscat : 2.2/3.5 Mm^{-1} , ΔIntV : 2.5/2.8 $\mu\text{m}^3 \text{cm}^{-3}$, and $\Delta N_{>3\mu\text{m}}$: 0.3/0.5 cm^{-3} , for strong/weak regimes).
405 The third hypothesis was that cloud drop number concentration ($3 < D_p < 50 \mu\text{m}$; N_d) would be greater in strong
406 coupling conditions, as stronger updrafts and turbulence would help to activate more particles into cloud droplets (this
407 was also found in Dong et al., 2015). This is confirmed in Table 3: mean N_d : 344/275 cm^{-3} for strong/weak regimes for
408 ACB legs coinciding with each MinAlt-BCB pair. This result is consistent with past studies for the northwest Atlantic
409 linking stronger turbulence to greater droplet activation efficiency (Kirschler et al., 2022; Dadashazar et al., 2021).
410 The results based on medians agree with those of mean values in Table 3, although medians across regimes for each
411 atmospheric property were not statistically different from one another (Fig. S2). [Although there is a lack of statistically](#)
412 [significant differences between the four coupling regimes for the investigated atmospheric properties, it is important](#)
413 [to note that the sample sizes for each regime vary greatly. Therefore, there is more variability within the weak coupling](#)
414 [regime with only 20 data points compared to the strong coupling regime with over 200 data points. As this study](#)
415 [utilized all of the data at its disposal and there were more strong coupling cases than any other coupling regime, the](#)
416 [lack of statistical significance across coupling regimes did not impact the general conclusions of the study.](#)

417

418 When comparing the moderate coupling regimes with the strong and weak regimes, neither Δ_{scat} , Δ_{IntV} , nor $\Delta_{N>3\mu\text{m}}$
 419 showed a consistent trend in terms of being higher or lower across all three variables. However, one consistent feature
 420 among the moderate regimes is that the moderate high Δ_{q_t} category showed smaller Δ values than moderate high $\Delta\theta_t$
 421 for the three aerosol variables. Sometimes, the lowest Δ values did not occur during the strong coupling cases, but
 422 rather during moderate coupling with high Δ_{q_t} cases (i.e., $\Delta_{\text{IntV}} = 1.9 \mu\text{m}^3 \text{ cm}^{-3}$, $\Delta_{N>3\mu\text{m}} = 0.2 \text{ cm}^{-3}$). These low
 423 differences presumably should coincide with the highest values of σ_w . This is somewhat supported by how BCB σ_w
 424 was greatest for the moderate coupling with high Δ_{q_t} regime ($0.81 \pm 0.76 \text{ m s}^{-1}$), although MinAlt σ_w was greatest for
 425 the moderate coupling with high $\Delta\theta_t$ regime ($1.00 \pm 0.57 \text{ m s}^{-1}$) with the value for the moderate coupling with high
 426 Δ_{q_t} regime being $0.81 \pm 0.44 \text{ m s}^{-1}$. Also, Appendix A provides discussion in support of why the high Δ_{q_t} category
 427 may have small aerosol differences between MinAlt and BCB levels, whereby surface effects may be at play to help
 428 promote mixing in the MBL. Interestingly, the highest N_d values were for the moderate high $\Delta\theta_t$ category with a mean
 429 of 419 cm^{-3} , which can partly be explained by how most of these cases occurred during the winter flights when N_d is
 430 higher than in the summer (see also Tables S2-S3) due to strong updraft velocities that efficiently activate particles
 431 into droplets (e.g., Kirschler et al., 2022). These conditions in winter were common during cold air outbreaks
 432 (Dadashazar et al., 2021).

433

434 3.3 Cloud Water Species

435 67 cloud water samples were used in this study (Table 4), with 60% of the samples falling into the strong coupling
 436 regime, followed by moderate coupling with high $\Delta\theta_t$ (25%), weak coupling (9%), and lastly moderate coupling with
 437 high Δ_{q_t} (6%). Locations of samples are shown in Fig. 3. Within the strong coupling and moderate coupling with high
 438 $\Delta\theta_t$ categories, there were several samples north of 37.5°N (marked by orange line in Fig. 3), whereas the moderate
 439 coupling with high Δ_{q_t} and weak coupling samples were all south of that latitude. The former two categories include
 440 substantially more data during the winter when air masses typically come from the continent featuring urban emissions
 441 (Dadashazar et al., 2022a).

442

443 **Table 4: Average cloud water mass concentrations ($\mu\text{g m}^{-3}$) and mass fractions (in %, rounded to nearest whole number)**
 444 **for all cloud water samples. Also shown are the pH and Cl:Na⁺ mass ratios. Results are categorized into different degrees**
 445 **of coupling, and the ratio of weak-to-strong coupling is also reported.**

446

| | Strong | Moderate, high $\Delta\theta_t$ | Moderate, high Δ_{q_t} | Weak | Weak : Strong |
|---|--------|------------------------------------|---|-------|---------------|
| Mass concentration ($\mu\text{g m}^{-3}$) | | | | | |
| Total | 87.45 | 57.93 | 91.92 | 10.32 | 0.12 |
| Cl ⁻ | 45.6 | 32.0 | 52.2 | 4.1 | 0.09 |
| Na ⁺ | 27.9 | 18.6 | 29.9 | 2.5 | 0.09 |
| Mg ²⁺ | 3.33 | 2.22 | 3.59 | 0.35 | 0.10 |
| K ⁺ | 0.56 | 0.37 | 0.59 | 0.05 | 0.09 |

| | | | | | |
|--------------------------------------|------|------|------|------|------|
| nss-Ca ²⁺ | 0.53 | 0.18 | 0.17 | 0.03 | 0.06 |
| nss-SO ₄ ²⁻ | 2.6 | 1.5 | 1.7 | 1.2 | 0.47 |
| NO ₃ ⁻ | 6.0 | 2.7 | 3.3 | 1.5 | 0.26 |
| Oxalate | 0.10 | 0.01 | 0.03 | 0.01 | 0.14 |
| NH ₄ ⁺ | 0.89 | 0.37 | 0.33 | 0.56 | 0.63 |
| Mass fraction (%) | | | | | |
| Cl ⁻ | 52 | 55 | 57 | 40 | 1 |
| Na ⁺ | 32 | 32 | 33 | 24 | 1 |
| Mg ²⁺ | 4 | 4 | 4 | 3 | 1 |
| K ⁺ | 1 | 1 | 1 | 1 | 1 |
| nss-Ca ²⁺ | 1 | 0 | 0 | 0 | 1 |
| nss-SO ₄ ²⁻ | 3 | 3 | 2 | 12 | 4 |
| NO ₃ ⁻ | 7 | 5 | 4 | 15 | 2 |
| Oxalate | 0 | 0 | 0 | 0 | 1 |
| NH ₄ ⁺ | 1 | 1 | 0 | 5 | 5 |
| Cl:Na ⁺ mass ratio and pH | | | | | |
| pH | 4.92 | 4.60 | 5.29 | 4.44 | 0.90 |
| Cl:Na ⁺ | 1.65 | 1.66 | 1.69 | 1.53 | 0.92 |
| n | 40 | 17 | 4 | 6 | |

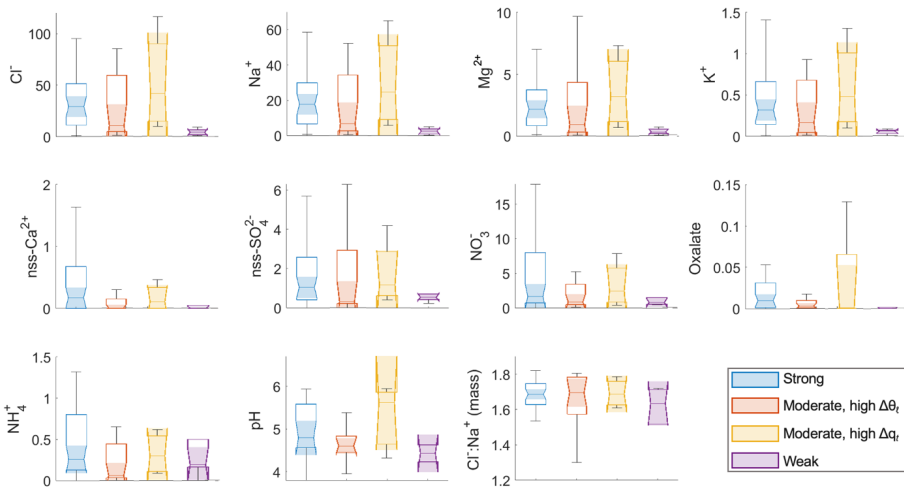
447
 448 Figure 5 provides composition statistics for the cloud water samples categorized into the four coupling regimes. As a
 449 note, the notches of the box plots assist in the determination of statistical significance between multiple medians (the
 450 shading indicates where the notches begin and end). If notches/shading do not overlap, the medians are statistically
 451 different from one another (also referred to as statistically significant). Since this study has utilized means instead of
 452 medians when comparing values across coupling regimes, mean concentrations are provided in the SI (Tables S4-S6)
 453 and the results of Welch's t-tests for each category (mean cloud water concentrations of the nine chemical species, pH,
 454 and Cl:Na⁺) are given in Table S7. This study also investigated cumulative average mass concentrations and mass
 455 fractions (Table 4) to paint a clearer picture of the breakdown of chemical species for different degrees of coupling.
 456 Based on previous work for stratocumulus clouds over the northeast Pacific (Wang et al., 2016), we hypothesize that
 457 samples from strong coupling regimes would have higher mass concentrations compared to weakly coupled regimes
 458 owing to higher concentrations of sea salt constituents (e.g., Cl⁻, Na⁺, Mg²⁺, and K⁺). More turbulent conditions in
 459 strongly coupled cases are thought to promote more mixing of sea salt into boundary layer clouds, which can be
 460 detected with cloud water composition measurements (e.g., Dadashazar et al., 2017).
 461

Deleted: (and shading)

Deleted: help to compare air-equivalent mass concentration medians across the different coupling categories and aid

Deleted: .

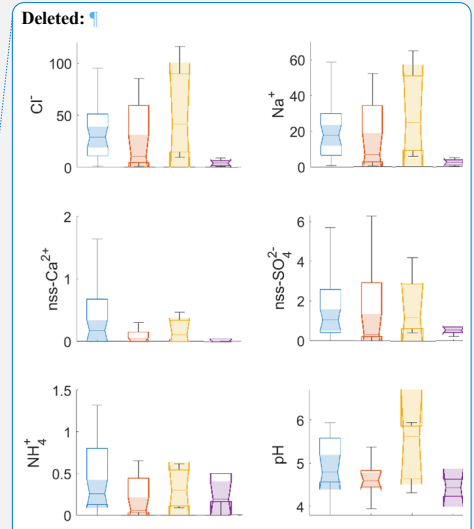
Formatted: Font: 9 pt



466
467 **Figure 5: Notched box plots of species concentrations ($\mu\text{g m}^{-3}$), $\text{Cl}^-:\text{Na}^+$ mass ratio, and pH from cloud water samples**
468 **collected during periods coinciding with MinAlt-BCB pairs.**

469
470 Strong coupling regime samples exhibit higher average mass concentrations compared to weak coupling, and Na^+ , Cl^-
471 , K^+ , and NO_3^- were all found to be statistically different across the two regimes (p-values: 1.07E^{-4} , 3.54E^{-5} , 5.52E^{-5} ,
472 and 9.57E^{-3} , respectively). The most abundant species by mass across the coupling regimes were usually Cl^- , Na^+ , and
473 NO_3^- , similar to the results of Wang et al. (2016). Further, although lower in absolute mass concentration, some species
474 were relatively more abundant (i.e., higher mass fraction) in the weak coupling regime: nss-SO_4^{2-} (12% [weak] vs. 3%
475 [strong]), NO_3^- (15% [weak] vs. 7% [strong]), NH_4^+ (5% [weak] vs. 1% [strong]). Oxalate was very low in overall
476 concentration and exhibited comparable mass fractions. These results are consistent with the idea of surface emissions
477 (mainly sea salt) driving cloud water composition in turbulent conditions (i.e., strongly coupled) in contrast to weakly
478 coupled clouds that have much lower overall mass concentrations of the reported ions but relatively more influence
479 from non-sea salt species. The two moderate coupling regimes include samples with concentration and mass fraction
480 values more similar to the strongly coupled regime, with even higher sea salt tracer species concentrations for the
481 moderate high Δq_i regime. This is consistent with the aerosol results in Sect. 3.2 that suggest this latter category can
482 have appreciable influence from the surface, although it is also important to note that this is based on 4 cloud water
483 samples.

484
485 Wang et al. (2016) analyzed 35 cloud water constituents for northeast Pacific stratocumulus clouds and found that 27
486 chemical species were higher in coupled clouds, with the remaining eight (acetate, formate, Si, NO_2^- , Al, Mn, Cr, and
487 Co) higher in decoupled clouds due to relatively more continental influence. The 27 cloud water species that were
488 higher in coupled clouds were associated with a mix of anthropogenic and natural sources (i.e., sea salt emissions for
489 Cl^- and Na^+). Conversely, the eight species that were higher in decoupled clouds were associated with crustal matter



Deleted: The box plots are colored according to degree of coupling: blue (strong), red (moderate, high $\Delta\theta_i$), yellow (moderate, high Δq_i), and purple (weak). The notches of the boxes assist in the determination of statistical significance between multiple medians (the shading indicates where the notches begin and end). If notches/shading do not overlap, the medians are statistically different from one another (also referred to as statistically significant). Table S7 provides the results of Welch's t-tests, which compares the means of two groups and determines if they are statistically different. The tests were performed on the mean cloud water concentrations of these nine chemical species, pH, and $\text{Cl}^-:\text{Na}^+$.

506 and biogenic sources. Several of the most abundant species from our study (Na^+ , Cl^- , Mg^{2+}) are common sea salt
507 tracers, while NO_3^- sources in the region may include ocean sea spray and biogenic emissions, wildfires, agricultural
508 emissions, and ship exhaust (Corral et al., 2020; Corral et al., 2021; Corral et al., 2022; Shah et al., 2018). Note that
509 nitric acid can partition effectively into cloud droplets as well, which can drive up cloud water NO_3^- levels (e.g.,
510 Prabhakar et al., 2014). At least some of the species with higher mass fractions in the weakly coupled regime (e.g.,
511 nss-SO_4^{2-} , NO_3^-) have previously been linked to combustion sources in this region, such as industrial emissions and
512 transportation (Brock et al., 2008; Song et al., 2001). Ammonium is a major base forming salts with nss-SO_4^{2-} and
513 NO_3^- , whereas oxalate has diverse sources (e.g., continental, marine) and can be associated with sea salt and produced
514 via cloud processing (e.g., Stahl et al., 2020; Hilario et al., 2021). nss-Ca^{2+} is often associated with continental crustal
515 matter (Ma et al., 2021; Edwards et al., 2024), and its concentrations are generally very low suggestive of low influence
516 from dust during the majority of ACTIVATE flights.

517
518 In addition to examining mass concentrations, we also examined pH and the $\text{Cl}^-:\text{Na}^+$ ratio. Regarding the latter ratio, sea
519 salt chloride concentrations can be reduced in the presence of acidic species such as sulfuric and nitric acids (e.g.,
520 Braun et al., 2017; Edwards et al., 2024). This phenomenon is known as Cl^- depletion, and it can be calculated by
521 taking the ratio of $\text{Cl}^-:\text{Na}^+$. For context, Wang et al. (2016) reported no major difference in the $\text{Cl}^-:\text{Na}^+$ ratio in cloud
522 water over the northeast Pacific but measured lower pH in coupled clouds (4.26) versus decoupled clouds (4.48). In
523 this study, samples in the weak coupling regime exhibited the lowest pH (4.4 vs. 5.0 for strong coupling) and $\text{Cl}^-:\text{Na}^+$
524 (1.5 vs. 1.7 for strong coupling), which potentially could be related to the higher relative amount of nss-SO_4^{2-} , NO_3^- .
525 The two moderate coupling regimes feature samples with pH and $\text{Cl}^-:\text{Na}^+$ values more similar to strongly coupled
526 samples.

527
528 A limitation in this analysis is that there were only six cloud water samples that fell into the weak coupling regime.
529 Future work examining the sensitivity of aerosol and cloud characteristics to coupling regimes should try to obtain
530 better sampling coverage across all regimes.

531
532 **4 Conclusions**
533 This study used data collected during the NASA ACTIVATE mission (2020–2022) from the HU-25 Falcon to assess
534 the frequency of different degrees of MBL cloud coupling and also how aerosol and cloud characteristics varied among
535 four such regimes. MinAlt and BCB legs were used to assess thermodynamic statistics along with turbulence, aerosol,
536 and cloud variables, which were calculated at each leg and the differences of the two legs were taken for final
537 comparison metrics. Cloud water species and N_d values associated with MinAlt and BCB pairs were analyzed when
538 cloud sampling occurred within 30 minutes of a MinAlt-BCB pair.

539
540 Vertical profiles between MinAlt and BCB pairs were divided into four degrees of coupling: strongly coupled ($\Delta q_r \leq$
541 0.8 g kg^{-1} , $\Delta \theta_r \leq 1.0 \text{ K}$), moderately coupled with high $\Delta \theta_r$ ($\Delta q_r \leq 0.8 \text{ g kg}^{-1}$, $\Delta \theta_r > 1.0 \text{ K}$), moderately coupled with
542 high Δq_r ($\Delta q_r > 0.8 \text{ g kg}^{-1}$, $\Delta \theta_r \leq 1.0 \text{ K}$), and weakly coupled ($\Delta q_r > 0.8 \text{ g kg}^{-1}$, $\Delta \theta_r > 1.0 \text{ K}$). In total, 411 MinAlt-BCB

543 pairs were investigated, along with 67 cloud water samples. Using this coupling categorization criteria, only a handful
544 of weakly coupled MBL clouds were detected (20, compared to 286 with strong coupling). The relative amounts of
545 the regimes did not vary substantially between the winter and summer seasons. Instead, particular focus was placed
546 on comparing regimes with strong coupling to those with weak coupling. Support for the coupling criteria was sought
547 through five different aerosol/cloud/dynamic parameters (Δscat , ΔIntV , $\Delta\text{N}_{>3\mu\text{m}}$, N_d , and σ_w) and 11 cloud water
548 variables (nss- Ca^{2+} , Cl^- , K^+ , Mg^{2+} , Na^+ , NH_4^+ , NO_3^- , oxalate, nss- SO_4^{2-} , pH, $\text{Cl}:\text{Na}^+$). Turbulence was generally greater
549 during regimes of strong coupling compared to weak coupling, which corresponded to lower values of Δscat , ΔIntV ,
550 and $\Delta\text{N}_{>3\mu\text{m}}$ due to better presumed mixing in the MBL. N_d was higher for strong coupling regimes, as higher
551 turbulence likely encouraged more cloud drop activation, which was also observed in Dong et al. (2015) for the
552 northeast Atlantic. Sea salt tracers (e.g., Na^+ , Cl^- , and K^+) were higher in concentration in strongly coupled compared
553 to weakly coupled MBL clouds and were found to have statistically significant differences across the two coupling
554 regimes. Additionally, nss- SO_4^{2-} , NO_3^- , and NH_4^+ , which are linked to continental sources, were found in higher mass
555 fractions during weak coupling regimes; this was also observed in Wang et al. (2016) for northeast Pacific
556 stratocumulus clouds, corresponding to lower values of both cloud water pH and the $\text{Cl}:\text{Na}^+$ ratio.

557
558 The inclusion of two moderate coupling categories is shown to be insightful as differences between the two potentially
559 can be explained by the relative influence of subsidence/entrainment versus surface effects. More specifically, the
560 moderately coupled category with high $\Delta\theta_t$ is thought to be influenced more by processes above the MBL such as
561 entrainment of dry air with high potential temperature whereas the other moderate category with high Δq_t likely has
562 more influence from surface processes. These speculations are supported by how the moderate high Δq_t regime
563 exhibited even more turbulent mixing than the strong coupling regime, yielding the highest sea salt concentrations in
564 cloud water and the lowest values of ΔIntV and $\Delta\text{N}_{>3\mu\text{m}}$. Furthermore, the moderate high $\Delta\theta_t$ category exhibited the
565 highest mean N_d value (419 cm^{-3}) of any category ($275\text{--}344\text{ cm}^{-3}$ for the other three categories), which can be explained
566 partly by how most of these cases (44 of 56) were in winter flights when N_d is typically higher than summer, especially
567 during cold air outbreaks (e.g., Dadashazar et al., 2021).

568
569 This study is the first to our knowledge to investigate degrees of coupling in MBL clouds through thermodynamic
570 statistics in the northwest Atlantic with a focus on aerosol and cloud microphysical characteristics. Further research
571 of this nature is needed in other regions to assess thermodynamic criteria for MBL cloud to surface coupling, including
572 how aerosol and cloud characteristics change with degrees of MBL coupling in different regions. The results here
573 indicate that a failure to account for different coupling regimes can mix together varying aerosol and cloud
574 microphysical characteristics in data analysis studies, which increases risk of separating out important details such as
575 how cloud composition is very different across the spectrum of cloud coupling strength. A limitation of this study to
576 build on is obtaining more statistics for the more weakly coupled category, which in part may be influenced by how
577 flight plans are designed. The results of this research have important implications for studies of aerosol-cloud
578 interactions, as not considering coupling strength will make interpretations difficult, as we have shown important
579 differences for aerosol and cloud properties.

580

581 **Appendix A. Discussion of the two moderate regimes**

582 To help with the interpretation of the two moderate regimes defined in Table 1, we provide a perspective based on the
583 following discussion. Using equation 1 but expanding it to take the difference of the liquid water potential temperature
584 between the BCB and MinAlt flight legs yields the following:

$$585 \Delta\theta_\ell = (\theta_{BCB} - \left(\frac{L_v}{c_{pd}}\right) \times q_{\ell,BCB}) - (\theta_{MinAlt} - \left(\frac{L_v}{c_{pd}}\right) \times q_{\ell,MinAlt}) \quad (A1)$$

586 Note that both q_ℓ terms are small below cloud. The $\Delta\theta_\ell$ value can thus be large due to large-scale subsidence or
587 entrainment when dry air from free troposphere with high θ which is potentially mixed with air at the BCB level.
588 While θ_{MinAlt} can be high due to surface heating, it acts to reduce $\Delta\theta_\ell$. Also, the current MinAlt is slightly above the
589 typical surface layer and hence the surface inversion. Also, note that:

$$590 \Delta q_t = (q_{v,MinAlt} + q_{l,MinAlt}) - (q_{v,BCB} + q_{l,BCB}) \quad (A2)$$

591 where both q_l terms are small below cloud and are typically much smaller than q_v . The range of q_v is largely controlled
592 by the temperature due to the Clapeyron-Clausius equation (the higher temperature, the higher saturation vapor
593 pressure). While high Δq_t may be due to low q_v at the BCB level, it is more likely due to high q_v near the surface
594 because saturation vapor pressure exponentially increases with temperature.

595 To conclude, the $\Delta\theta_\ell$ term is more likely influenced by features above the MBL while the Δq_t term is more likely
596 influenced by near-surface effects.

597

598 **Data availability**

599 The ACTIVATE dataset can be downloaded at <https://doi.org/10.5067/SUBORBITAL/ACTIVATE/DATA001>
600 (ACTIVATE Science Team, 2020).

601

602 **Author contributions**

603 YC, EC, JPD, GSD, MAF, SK, JBN, MAS, KLT, CV, ELW, and LDZ collected and/or prepared the data. KTZ, SD,
604 and KM conducted data analysis. KTZ, KM, and SD conducted the formal investigation. KTZ, LWS, and AS
605 conducted data interpretation. KTZ and AS prepared the manuscript with editing from all co-authors.

606

607 **Competing interests**

608 At least one of the (co-)authors is a member of the editorial board of Atmospheric Chemistry and Physics.

609

610 **Disclaimer**

611 Publisher's note: Copernicus Publications remains neutral with regard to jurisdictional claims in published maps and
612 institutional affiliations.

613

614 **Acknowledgements**

615 We thank the pilots and aircraft maintenance personnel of NASA Langley Research Services Directorate for
616 conducting ACTIVATE flights and all others who were involved in executing the ACTIVATE campaign.

617

618 **Financial support**

619 ACTIVATE is a NASA Earth Venture Suborbital-3 (EVS-3) investigation funded by NASA's Earth Science Division
620 and managed through the Earth System Science Pathfinder Program Office. University of Arizona investigators were
621 supported by NASA grant no. 80NSSC19K0442 and ONR grant no. N00014-21-1-2115. CV and SK were funded by
622 DFG SPP-1294 HALO under project no. 522359172 and by the European Union's Horizon Europe program through
623 the Single European Sky ATM Research 3 Joint Undertaking projects CONCERTO (grant no 101114785) and
624 CICONIA (grant no 101114613).

625 **References**

- 626 ACTIVATE Science Team: Aerosol Cloud Meteorology Interactions oVer the western ATlantic Experiment Data,
627 <https://doi.org/10.5067/SUBORBITAL/ACTIVATE/DATA001>, 2020.
- 628 Andreae, M. O., Elbert, W., Cai, Y., Andreae, T. W., and Gras, J.: Non-sea-salt sulfate, methanesulfonate, and nitrate
629 aerosol concentrations and size distributions at Cape Grim, Tasmania, *Journal of Geophysical Research:*
630 *Atmospheres*, 104, 21695-21706, <https://doi.org/10.1029/1999JD900283>, 1999.
- 631 Ayers, G. P., Ivey, J. P., and Gillett, R. W.: Coherence between seasonal cycles of dimethyl sulphide,
632 methanesulphonate and sulphate in marine air, *Nature*, 349, 404-406, <https://doi.org/10.1038/349404a0>, 1991.
- 633 AzadiAghdam, M., Braun, R. A., Edwards, E.-L., Bañaga, P. A., Cruz, M. T., Betito, G., Cambaliza, M. O.,
634 Dadashazar, H., Lorenzo, G. R., Ma, L., MacDonald, A. B., Nguyen, P., Simpas, J. B., Stahl, C., and Sorooshian,
635 A.: On the nature of sea-salt aerosol at a coastal megacity: Insights from Manila, Philippines in Southeast Asia,
636 *Atmospheric Environment*, 216, 116922, <https://doi.org/10.1016/j.atmosenv.2019.116922>, 2019.
- 637 Bretherton, C. S. and Wyant, M. C.: Moisture transport, lower-tropospheric stability, and decoupling of cloud-topped
638 boundary layers, *Journal of the Atmospheric Sciences*, 54, 148-167, [https://doi.org/10.1175/1520-0469\(1997\)054<0148:MTLTA>2.0.CO;2](https://doi.org/10.1175/1520-0469(1997)054<0148:MTLTA>2.0.CO;2), 1997.
- 640 Bretherton, C. S., Wood, R., George, R. C., Leon, D., Allen, G., and Zheng, X.: Southeast Pacific stratocumulus clouds,
641 precipitation and boundary layer structure sampled along 20° S during VOCALS-REx, *Atmospheric Chemistry*
642 *and Physics*, 10, 10639-10654, <https://doi.org/10.5194/acp-10-10639-2010>, 2010.
- 643 Brock, C.A., Sullivan, A.P., Peltier, R.E., Weber, R.J., Wollny, A., De Gouw, J.A., Middlebrook, A.M., Atlas, E.L.,
644 Stohl, A., Trainer, M.K. and Cooper, O.R.: Sources of particulate matter in the northeastern United States in
645 summer: 2. Evolution of chemical and microphysical properties, *Journal of Geophysical Research:*
646 *Atmospheres*, 113, D8, <https://doi.org/10.1029/2007JD009241>, 2008.
- 647 Brümmer, B.: Boundary layer mass, water, and heat budgets in wintertime cold-air outbreaks from the Arctic sea ice,
648 *Monthly Weather Review*, 125, 1824-1837, [https://doi.org/10.1175/1520-0493\(1997\)125<1824:BLMWAH>2.0.CO;2](https://doi.org/10.1175/1520-0493(1997)125<1824:BLMWAH>2.0.CO;2), 1997.
- 650 Brunke, M. A., Cutler, L., Urzua, R. D., Corral, A. F., Crosbie, E., Hair, J., Hostetler, C., Kirschler, S., Larson, V., Li,
651 X.-Y., Ma, P.-L., Minke, A., Moore, R., Robinson, C. E., Scarino, A. J., Schlosser, J., Shook, M., Sorooshian, A.,
652 Thornhill, K. L., Voigt, C., Wan, H., Wang, H., Winstead, E., Zeng, X., Zhang, S., and Ziemba, L. D.: Aircraft
653 observations of turbulence in cloudy and cloud-free boundary layers over the western North Atlantic Ocean from
654 ACTIVATE and implications for the Earth system model evaluation and development, *Journal of Geophysical*
655 *Research: Atmospheres*, 127, e2022JD036480, <https://doi.org/10.1029/2022JD036480>, 2022.
- 656 Corral, A.F., Dadashazar, H., Stahl, C., Edwards, E.-L., Zuidema, P., and Sorooshian, A.: Source apportionment of
657 aerosol at a coastal site and relationships with precipitation chemistry: A case study over the southeast united
658 states, *Atmosphere*, 11, 1212, <https://doi.org/10.3390/atmos11111212>, 2020.
- 659 Corral, A. F., Braun, R. A., Cairns, B., Gorooh, V. A., Liu, H., Ma, L., Mardi, A. H., Painemal, D., Starnes, S., van
660 Diedenhoven, B., Wang, H., Yang, Y., Zhang, B., and Sorooshian, A.: An overview of atmospheric features over
661 the western north Atlantic ocean and North American east coast – Part 1: Analysis of aerosols, gases, and wet

662 deposition chemistry, *Journal of Geophysical Research: Atmospheres*, 126, e2020JD032592,
663 <https://doi.org/10.1029/2020JD032592>, 2021.

664 Corral, A. F., Choi, Y., Collister, B. L., Crosbie, E., Dadashazar, H., DiGangi, J. P., Diskin, G. S., Fenn, M., Kirschler,
665 S., Moore, R. H., Nowak, J. B., Shook, M. A., Stahl, C. T., Shingler, T., Thornhill, K. L., Voigt, C., Ziemba, L.
666 D., and Sorooshian, A.: Dimethylamine in cloud water: a case study over the northwest Atlantic Ocean,
667 *Environmental Science: Atmospheres*, 2, 1534-1550, <https://doi.org/10.1039/d2ea00117a>, 2022.

668 Crosbie, E., Brown, M. D., Shook, M., Ziemba, L., Moore, R. H., Shingler, T., Winstead, E., Thornhill, K. L.,
669 Robinson, C., MacDonald, A. B., Dadashazar, H., Sorooshian, A., Beyersdorf, A., Eugene, A., Collett Jr, J.,
670 Straub, D., and Anderson, B.: Development and characterization of a high-efficiency, aircraft-based axial cyclone
671 cloud water collector, *Atmospheric Measurement Techniques*, 11, 5025-5048, [https://doi.org/10.5194/amt-11-](https://doi.org/10.5194/amt-11-5025-2018)
672 [5025-2018](https://doi.org/10.5194/amt-11-5025-2018), 2018.

673 Dadashazar, H., Wang, Z., Crosbie, E., Brunke, M., Zeng, X., Jonsson, H., Woods, R. K., Flagan, R. C., Seinfeld, J.
674 H., and Sorooshian, A.: Relationships between giant sea salt particles and clouds inferred from aircraft
675 physicochemical data, *Journal of Geophysical Research Atmospheres*, 122, 3421–3434,
676 <https://doi.org/10.1002/2016JD026019>, 2017.

677 Dadashazar, H., Painemal, D., Alipanah, M., Brunke, M., Chellappan, S., Corral, A. F., Crosbie, E., Kirschler, S., Liu,
678 H., Moore, R. H., Robinson, C., Scarino, A. J., Shook, M., Sinclair, K., Thornhill, K. L., Voigt, C., Wang, H.,
679 Winstead, E., Zeng, X., Ziemba, L., Zuidema, P., and Sorooshian, A.: Cloud drop number concentrations over the
680 western North Atlantic Ocean: seasonal cycle, aerosol interrelationships, and other influential factors,
681 *Atmospheric Chemistry and Physics*, 21, 10499-10526, <https://doi.org/10.5194/acp-21-10499-2021>, 2021.

682 Dadashazar, H., Corral, A. F., Crosbie, E., Dmitrovic, S., Kirschler, S., McCauley, K., Moore, R., Robinson, C.,
683 Schlosser, J. S., Shook, M., Thornhill, K. L., Voigt, C., Winstead, E., Ziemba, L., and Sorooshian, A.: Organic
684 enrichment in droplet residual particles relative to out of cloud over the northwestern Atlantic: analysis of airborne
685 ACTIVATE data, *Atmospheric Chemistry and Physics*, 22, 13897-13913, [https://doi.org/10.5194/acp-22-13897-](https://doi.org/10.5194/acp-22-13897-2022)
686 [2022](https://doi.org/10.5194/acp-22-13897-2022), 2022a

687 Dadashazar, H.; Crosbie, E.; Choi, Y.; Corral, A.F.; DiGangi, J.P.; Diskin, G.S.; Dmitrovic, S.; Kirschler, S.; McCauley,
688 K.; Moore, R.H.; et al.: Analysis of MONARC and ACTIVATE airborne aerosol data for aerosol-cloud interaction
689 investigations: Efficacy of stairstepping flight legs for airborne in situ sampling, *Atmosphere*, 13, 1242,
690 <https://doi.org/10.3390/atmos13081242>, 2022b.

691 Diskin, G., Podolske, J., Sachse, G., and Slate, T.: Open-path airborne tunable diode laser hygrometer. *Society of*
692 *Photo-Optical Instrumentation Engineers*, 4817, <https://doi.org/10.1117/12.453736>, 2002.

693 Dong, X., Schwantes, A. C., Xi, B., and Wu, P.: Investigation of the marine boundary layer cloud and CCN properties
694 under coupled and decoupled conditions over the Azores, *Journal of Geophysical Research: Atmospheres*, 120,
695 6179-6191, <https://doi.org/10.1002/2014JD022939>, 2015.

696 Edwards, E. L., Choi, Y., Crosbie, E. C., DiGangi, J. P., Diskin, G. S., Robinson, C. E., Shook, M. A., Winstead, E. L.,
697 Ziemba, L. D., and Sorooshian, A.: Sea-salt reactivity over the northwest Atlantic: an in-depth look using the

698 airborne ACTIVATE dataset, *Atmospheric Chemistry and Physics*, 24, 3349-3378, 10.5194/acp-24-3349-2024,
699 2024.

700 Froyd, K. D., Murphy, D. M., Brock, C. A., Campuzano-Jost, P., Dibb, J. E., Jimenez, J. L., Kupc, A., Middlebrook,
701 A. M., Schill, G. P., Thornhill, K. L., Williamson, C. J., Wilson, J. C., and Ziemba, L. D.: A new method to
702 quantify mineral dust and other aerosol species from aircraft platforms using single-particle mass spectrometry.
703 *Atmospheric Measurement Techniques*, 12, 11, 6209-6239, <https://doi.org/10.5194/amt-12-6209-2019>, 2019.

704 Gonzalez, M. E., Corral, A. F., Crosbie, E., Dadashazar, H., Diskin, G. S., Edwards, E.-L., Kirschler, S., Moore, R.
705 H., Robinson, C. E., Schlosser, J. S., Shook, M., Stahl, C., Thornhill, K. L., Voigt, C., Winstead, E., Ziemba, L.
706 D., and Sorooshian, A.: Relationships between supermicrometer particle concentrations and cloud water sea-salt
707 and dust concentrations: analysis of MONARC and ACTIVATE data, *Environmental Science: Atmospheres*, 2,
708 738-752, <https://doi.org/10.1039/D2EA00049K>, 2022.

709 Goren, T., Rosenfeld, D., Sourdeval, O., and Quaas, J.: Satellite observations of precipitating marine stratocumulus
710 show greater cloud fraction for decoupled clouds in comparison to coupled clouds, *Geophysical Research Letters*,
711 45, 5126-5134, <https://doi.org/10.1029/2018GL078122>, 2018.

712 Griesche, H. J., Ohneiser, K., Seifert, P., Radenz, M., Engelmann, R., and Ansmann, A.: Contrasting ice formation in
713 Arctic clouds: surface-coupled vs. surface-decoupled clouds, *Atmospheric Chemistry and Physics*, 21, 10357-
714 10374, <https://doi.org/10.5194/acp-21-10357-2021>, 2021.

715 Hilario, M. R. A., Crosbie, E., Bañaga, P. A., Betito, G., Braun, R. A., Cambaliza, M. O., Corral, A. F., Cruz, M. T.,
716 Dibb, J. E., Lorenzo, G. R., MacDonald, A. B., Robinson, C. E., Shook, M. A., Simpas, J. B., Stahl, C., Winstead,
717 E., Ziemba, L. D., and Sorooshian, A.: Particulate oxalate-to-sulfate ratio as an aqueous processing marker:
718 Similarity across field campaigns and limitations, *Geophysical Research Letters*, 48, e2021GL096520,
719 <https://doi.org/10.1029/2021GL096520>, 2021.

720 Jones, C. R., Bretherton, C. S., and Leon, D.: Coupled vs. decoupled boundary layers in VOCALS-REx, *Atmospheric*
721 *Chemistry and Physics*, 11, 7143-7153, <https://doi.org/10.5194/acp-11-7143-2011>, 2011.

722 Kirschler, S., Voigt, C., Anderson, B., Campos Braga, R., Chen, G., Corral, A. F., Crosbie, E., Dadashazar, H., Ferrare,
723 R. A., Hahn, V., Hendricks, J., Kaufmann, S., Moore, R., Pöhlker, M. L., Robinson, C., Scarino, A. J.,
724 Schollmayer, D., Shook, M. A., Thornhill, K. L., Winstead, E., Ziemba, L. D., and Sorooshian, A.: Seasonal
725 updraft speeds change cloud droplet number concentrations in low-level clouds over the western North Atlantic.
726 *Atmospheric Chemistry and Physics*, 22, 12, 8299-8319, <https://doi.org/10.5194/acp-22-8299-2022>, 2022.

727 Kirschler, S., Voigt, C., Anderson, B. E., Chen, G., Crosbie, E. C., Ferrare, R. A., Hahn, V., Hair, J. W., Kaufmann, S.,
728 Moore, R. H., Painemal, D., Robinson, C. E., Sanchez, K. J., Scarino, A. J., Shingler, T. J., Shook, M. A.,
729 Thornhill, K. L., Winstead, E. L., Ziemba, L. D., and Sorooshian, A.: Overview and statistical analysis of
730 boundary layer clouds and precipitation over the western North-Atlantic Ocean. *EGUsphere*, 1-29.
731 <https://doi.org/10.5194/egusphere-2023-898>, 2023.

732 Korhonen, H., Carslaw, K. S., Spracklen, D. V., Mann, G. W., and Woodhouse, M. T.: Influence of oceanic dimethyl
733 sulfide emissions on cloud condensation nuclei concentrations and seasonality over the remote Southern

734 Hemisphere oceans: A global model study, *Journal of Geophysical Research: Atmospheres*, 113,
735 <https://doi.org/10.1029/2007JD009718>, 2008.

736 Ma, L., Dadashazar, H., Hilario, M. R. A., Cambaliza, M. O., Lorenzo, G. R., Simpas, J. B., Nguyen, P., and
737 Sorooshian, A.: Contrasting wet deposition composition between three diverse islands and coastal North
738 American sites, *Atmospheric Environment*, 244, 117919, <https://doi.org/10.1016/j.atmosenv.2020.117919>, 2021.

739 MacDonald, A. B., Hossein Mardi, A., Dadashazar, H., Azadi Aghdam, M., Crosbie, E., Jonsson, H. H., Flagan, R. C.,
740 Seinfeld, J. H., and Sorooshian, A.: On the relationship between cloud water composition and cloud droplet
741 number concentration. *Atmos. Chem. Phys.*, 20, 13, 7645-7665, <https://doi.org/10.5194/acp-20-7645-2020>, 2020.

742 McNaughton, C. S., Clarke, A. D., Howell, S. G., Pinkerton, M., Anderson, B., Thornhill, L., Hudgins, C., Winstead,
743 E., Dibb, J. E., Scheuer, E., and Maring, H.: Results from the DC-8 Inlet Characterization Experiment (DICE):
744 Airborne versus surface sampling of mineral dust and sea-salt aerosols, *Aerosol Science and Technology*, 41, 136-
745 159, <https://doi.org/10.1080/02786820601118406>, 2007.

746 Nicholls, S.: The dynamics of stratocumulus: Aircraft observations and comparisons with a mixed layer model,
747 *Quarterly Journal of the Royal Meteorological Society*, 110, 783-820, <https://doi.org/10.1002/qj.49711046603>,
748 1984.

749 Painemal, D., Corral, A. F., Sorooshian, A., Brunke, M. A., Chellappan, S., Afzali Goroooh, V., Ham, S.-H., O'Neill,
750 L., Smith Jr., W. L., Tselioudis, G., Wang, H., Zeng, X., and Zuidema, P.: An overview of atmospheric features
751 over the western North Atlantic ocean and North American east coast—Part 2: Circulation, boundary layer, and
752 clouds, *Journal of Geophysical Research: Atmospheres*, 126, e2020JD033423,
753 <https://doi.org/10.1029/2020JD033423>, 2021.

754 Painemal, D., Chellappan, S., Smith Jr., W. L., Spangenberg, D., Park, J. M., Ackerman, A., Chen, J., Crosbie, E.,
755 Ferrare, R., Hair, J., Kirschler, S., Li, X.-Y., McComiskey, A., Moore, R. H., Sanchez, K., Sorooshian, A., Tornow,
756 F., Voigt, C., Wang, H., Winstead, E., Zeng, X., Ziemba, L., and Zuidema, P.: Wintertime synoptic patterns of
757 midlatitude boundary layer clouds over the western North Atlantic: Climatology and insights from in situ
758 ACTIVATE observations, *Journal of Geophysical Research: Atmospheres*, 128, e2022JD037725,
759 <https://doi.org/10.1029/2022JD037725>, 2023.

760 Prabhakar, G., Ervens, B., Wang, Z., Maudlin, L. C., Coggon, M. M., Jonsson, H. H., Seinfeld, J. H., and Sorooshian,
761 A.: Sources of nitrate in stratocumulus cloud water: Airborne measurements during the 2011 E-PEACE and 2013
762 NiCE studies, *Atmospheric Environment*, 97, 166-173, <https://doi.org/10.1016/j.atmosenv.2014.08.019>, 2014.

763 Papritz, L. and Spengler, T.: Analysis of the slope of isentropic surfaces and its tendencies over the North Atlantic,
764 *Quarterly Journal of the Royal Meteorological Society*, 141, 3226-3238, <https://doi.org/10.1002/qj.2605>, 2015.

765 Ramanathan, V., Cess, R. D., Harrison, E. F., Minnis, P., Barkstrom, B. R., Ahmad, E., and Hartmann, D. Cloud-
766 radiative forcing and climate: Results from the Earth Radiation Budget Experiment. *Science*, 243, 4887, 57-63,
767 <https://doi.org/doi:10.1126/science.243.4887.57/>, 1989.

768 Seethala, C., Zuidema, P., Edson, J., Brunke, M., Chen, G., Li, X.-Y., Painemal, D., Robinson, C., Shingler, T., Shook,
769 M., Sorooshian, A., Thornhill, L., Tornow, F., Wang, H., Zeng, X., and Ziemba, L.: On assessing ERA5 and

770 MERRA2 representations of cold-air outbreaks across the Gulf Stream, *Geophysical Research Letters*, 48,
771 e2021GL094364, <https://doi.org/10.1029/2021GL094364>, 2021.

772 Shah, V., Jaeglé, L., Thornton, J. A., Lopez-Hilfiker, F. D., Lee, B. H., Schroder, J. C., Campuzano-Jost, P., Jimenez,
773 J. L., Guo, H., Sullivan, A.P., Weber, R. J., Green, J. R., Fiddler, M. N., Bililign, S., Campos, T. L., Stell, M.,
774 Weinheimer, A.J., Montzka, D. D., and Brown, S. S.: Chemical feedbacks weaken the wintertime response of
775 particulate sulfate and nitrate to emissions reductions over the eastern United States, *National Academy of
776 Sciences*, 115, 8110-8115, <https://doi.org/10.1073/pnas.1803295115>, 2018.

777 Song, X.H., Polissar, A.V. and Hopke, P.K.: Sources of fine particle composition in the northeastern US, *Atmospheric
778 Environment*, 35, 31, 5277-5286, [https://doi.org/10.1016/S1352-2310\(01\)00338-7](https://doi.org/10.1016/S1352-2310(01)00338-7), 2001.

779 Sorooshian, A., Anderson, B., Bauer, S. E., Braun, R. A., Cairns, B., Crosbie, E., Dadashazar, H., Diskin, G., Ferrare,
780 R., Flagan, R. C., Hair, J., Hostetler, C., Jonsson, H. H., Kleb, M. M., Liu, H., MacDonald, A. B., McComiskey,
781 A., Moore, R., Painemal, D., Russell, L. M., Seinfeld, J. H., Shook, M., Smith, W. L., Thornhill, K., Tselioudis,
782 G., Wang, H., Zeng, X., Zhang, B., Ziemba, L., and Zuidema, P.: Aerosol–cloud–meteorology interaction airborne
783 field investigations: Using lessons learned from the U.S. west coast in the design of ACTIVATE off the U.S. East
784 Coast, *Bulletin of the American Meteorological Society*, 100, 1511-1528, [https://doi.org/10.1175/BAMS-D-18-
785 0100.1](https://doi.org/10.1175/BAMS-D-18-0100.1), 2019.

786 Sorooshian, A., Alexandrov, M. D., Bell, A. D., Bennett, R., Betito, G., Burton, S. P., Buzanowicz, M. E., Cairns, B.,
787 Chemyakin, E. V., Chen, G., Choi, Y., Collister, B. L., Cook, A. L., Corral, A. F., Crosbie, E. C., van Dierenhoven,
788 B., DiGangi, J. P., Diskin, G. S., Dmitrovic, S., Edwards, E. L., Fenn, M. A., Ferrare, R. A., van Gilst, D., Hair, J.
789 W., Harper, D. B., Hilario, M. R. A., Hostetler, C. A., Jester, N., Jones, M., Kirschler, S., Kleb, M. M., Kusterer,
790 J. M., Leavor, S., Lee, J. W., Liu, H., McCauley, K., Moore, R. H., Nied, J., Notari, A., Nowak, J. B., Painemal,
791 D., Phillips, K. E., Robinson, C. E., Scarino, A. J., Schlosser, J. S., Seaman, S. T., Seethala, C., Shingler, T. J.,
792 Shook, M. A., Sinclair, K. A., Smith Jr, W. L., Spangenberg, D. A., Stamnes, S. A., Thornhill, K. L., Voigt, C.,
793 Vömel, H., Wasilewski, A. P., Wang, H., Winstead, E. L., Zeider, K., Zeng, X., Zhang, B., Ziemba, L. D., and
794 Zuidema, P.: Spatially coordinated airborne data and complementary products for aerosol, gas, cloud, and
795 meteorological studies: the NASA ACTIVATE dataset, *Earth Syst. Sci. Data*, 15, 3419-3472,
796 <https://doi.org/10.5194/essd-15-3419-2023>, 2023.

797 Stahl, C., Cruz, M. T., Bañaga, P. A., Betito, G., Braun, R. A., Aghdam, M. A., Cambaliza, M. O., Lorenzo, G. R.,
798 MacDonald, A. B., Hilario, M. R. A., Pabroa, P. C., Yee, J. R., Simpas, J. B., and Sorooshian, A.: Sources and
799 characteristics of size-resolved particulate organic acids and methanesulfonate in a coastal megacity: Manila,
800 Philippines, *Atmospheric Chemistry and Physics*, 20, 15907-15935, <https://doi.org/10.5194/acp-20-15907-2020>,
801 2020.

802

803 Stevens, B., Cotton, W. R., Feingold, G., and Moeng, C.-H.: Large-eddy simulations of strongly precipitating, shallow,
804 stratocumulus-topped boundary layers, *Journal of the Atmospheric Sciences*, 55, 3616-3638,
805 [https://doi.org/10.1175/1520-0469\(1998\)055<3616:LESOSP>2.0.CO;2](https://doi.org/10.1175/1520-0469(1998)055<3616:LESOSP>2.0.CO;2), 1998.

806 Su, T., Zheng, Y., and Li, Z.: Methodology to determine the coupling of continental clouds with surface and boundary
807 layer height under cloudy conditions from lidar and meteorological data, *Atmos. Chem. Phys.*, 22, 1453-1466,
808 <https://doi.org/10.5194/acp-22-1453-2022>, 2022.

809 Thornhill, K. L., Anderson, B. E., Barrick, J. D. W., Bagwell, D. R., Friesen, R., and Lenschow, D. H.: Air motion
810 intercomparison flights during Transport and Chemical Evolution in the Pacific (TRACE-P)/ACE-ASIA. *Journal*
811 *of Geophysical Research: Atmospheres*, 108, D20, <https://doi.org/10.1029/2002JD003108>, 2003.

812 Tornow, F., Ackerman, A. S., Fridlind, A. M., Cairns, B., Crosbie, E. C., Kirschler, S., Moore, R. H., Painemal, D.,
813 Robinson, C. E., Seethala, C., Shook, M. A., Voigt, C., Winstead, E. L., Ziemba, L. D., Zuidema, P., and
814 Sorooshian, A.: Dilution of boundary layer cloud condensation nucleus concentrations by free tropospheric
815 entrainment during marine cold air outbreaks. *Geophysical Research Letters*, 49, e2022GL098444,
816 <https://doi.org/10.1029/2022GL098444>, 2022.

817 Twomey, S.: Pollution and the planetary albedo, *Atmospheric Environment* (1967), 8, 1251-1256,
818 [https://doi.org/10.1016/0004-6981\(74\)90004-3](https://doi.org/10.1016/0004-6981(74)90004-3), 1974.

819 Wang, Z., Mora Ramirez, M., Dadashazar, H., MacDonald, A. B., Crosbie, E., Bates, K. H., Coggon, M. M., Craven,
820 J. S., Lynch, P., Campbell, J. R., Azadi Aghdam, M., Woods, R. K., Jonsson, H., Flagan, R. C., Seinfeld, J. H.,
821 and Sorooshian, A.: Contrasting cloud composition between coupled and decoupled marine boundary layer
822 clouds, *Journal of Geophysical Research: Atmospheres*, 121, 11,679-611,691,
823 <https://doi.org/10.1002/2016JD025695>, 2016.

824 Warren, S.G., Hahn, C.J., London, J., Chervin, R.M., Jenne, R.L.: Global distribution of total cloud cover and cloud
825 type amounts over the ocean. United States: n. p., <https://doi.org/10.2172/5415329>, 1988.

826 Ziemba, L. D., Lee Thornhill, K., Ferrare, R., Barrick, J., Beyersdorf, A. J., Chen, G., Crumeyrolle, S. N., Hair, J.,
827 Hostetler, C., Hudgins, C., Obland, M., Rogers, R., Scarino, A. J., Winstead, E. L., and Anderson, B. E.: Airborne
828 observations of aerosol extinction by in situ and remote-sensing techniques: Evaluation of particle hygroscopicity.
829 *Geophysical Research Letters*, 40, 2, 417-422, <https://doi.org/https://doi.org/10.1029/2012GL054428>, 2013.

830 Zuidema, P., Painemal, D., de Szoek, S., and Fairall, C.: Stratocumulus cloud-top height estimates and their climatic
831 implications, *Journal of Climate*, 22, 4652-4666, <https://doi.org/10.1175/2009JCLI2708.1>, 2009.